Displacement monitoring and modelling of a high-speed railway bridge using C-band Sentinel-1 data

Qihuan Huang [a], Michele Crosetto [b,*], Oriol Monserrat [b], Bruno Crippa [c]

[a] School of Earth Sciences and Engineering, Hohai University, Jiangning District, 211100 Nanjing, China
[b] Centre Tecnològic de Telecomunicacions de Catalunya (CTTC), Geomatics Division, Castelldefels, Spain
[c] Department of Earth Sciences, Section of Geophysics, University of Milan, Via Cicognara 7, I-20129 Milan, Italy

ABSTRACT

Bridge displacement monitoring is one of the key components of bridge structural health monitoring. Traditional methods, usually based on limited sets of sensors mounted on a given bridge, collect point-like deformation information and have the disadvantage of providing incomplete displacement information. In this paper, a Persistent Scatterer Interferometry (PSI) approach is used to monitor the displacements of the Nanjing Dashengguan Yangtze River high-speed railway bridge. Twenty-nine (29) European Space Agency Sentinel-1A images, acquired from April 25, 2015 to August 5, 2016, were used in the PSI analysis. A total of 1828 measurement points were selected on the bridge. The results show a maximum longitudinal displacement of about 150 mm on each side of the bridge. The measured displacements showed a strong correlation with the environmental temperature at the time the images used were acquired, indicating that they were due to thermal expansion of the bridge. At each pier, a regression model based on the PSI-measured displacements was compared with a model based on in-situ measurements. The good agreement of these models demonstrates the capability of the PSI technique to monitor long-span railway bridge displacements. By comparing the modelled displacements and dozens of PSI measurements, we show how the performance of movable bearings can be evaluated. The high density of the PSI measurement points is advantageous for the health monitoring of the entire bridge.
© 2017 International Society for Photogrammetry and Remote Sensing, Inc. (ISPRS). Published by Elsevier B.V. All rights reserved.

1. Introduction

The object of this study is the Nanjing Dashengguan Yangtze River high-speed railway bridge. The main bridge is supported by three movable bearings on each side, named 4#, 5#, 6# on the northwest side and 8#, 9#, 10# on the southeast side, while a fixed bearing is mounted at 7# (see Figs. 1 and 2). It is necessary to monitor and evaluate the status of the movable bearings for the safe operation of the entire bridge. At present, two displacement monitoring methods are commonly used. One is an in-situ measurement periodically performed by workers, which is highly subjective and has no real-time capability. The other is the installation of displacement sensors to monitor the longitudinal displacement at each pier, which can take and store real-time measurements. Based on these measurements, a displacement model can be established and used to evaluate the state of the

movable bearings. For instance, an abnormal change in the longitudinal displacements at a given pillar can indicate a problem with the corresponding movable bearing (de Battista et al., 2011; Wang et al., 2016; Webb et al., 2014; Yi et al., 2010). The main limitation of the latter method is that it can only monitor the displacements in correspondence of each pillar.

Interferometric Synthetic Aperture Radar (InSAR) is a powerful satellite-based technique to measure land deformation, e.g. see (Liu et al., 2016; Wen et al., 2016). The Persistent Scatterer Interferometry (PSI) technique (Ferretti et al., 2001; Crosetto et al., 2016) is an advanced class of the InSAR techniques. Examples of PSI applications include landslide monitoring (Crosetto et al., 2013), subsidence monitoring in urban areas (Dai et al., 2015; Tosi et al., 2016), linear infrastructures (Lin et al., 2010), etc. In recent years, the displacements caused by thermal expansion have been studied by PSI (Eineder et al., 2009; Gernhardt et al., 2010). As far as the thermal expansion of bridges monitored by PSI is concerned, several authors (Crosetto et al., 2008, 2010; Cuevas et al., 2011; Fornaro et al., 2013; Goel et al., 2014; Lazecky et al., 2016; Monserrat et al., 2011; Perissin and Rocca, 2006; Reale et al., 2013) have dealt
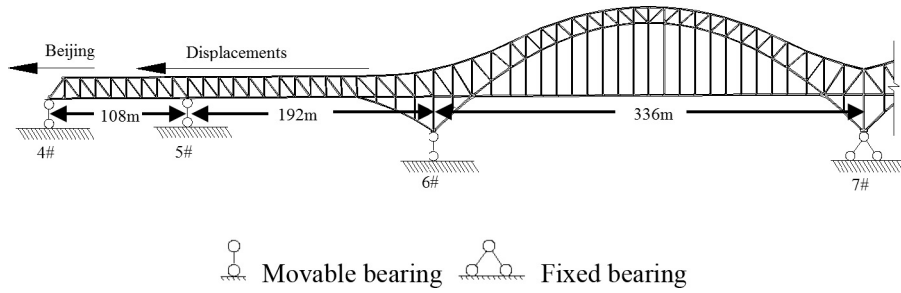
Fig. 1. Schematic of the high-speed railway bridge studied.


(a)   (b)

(c)
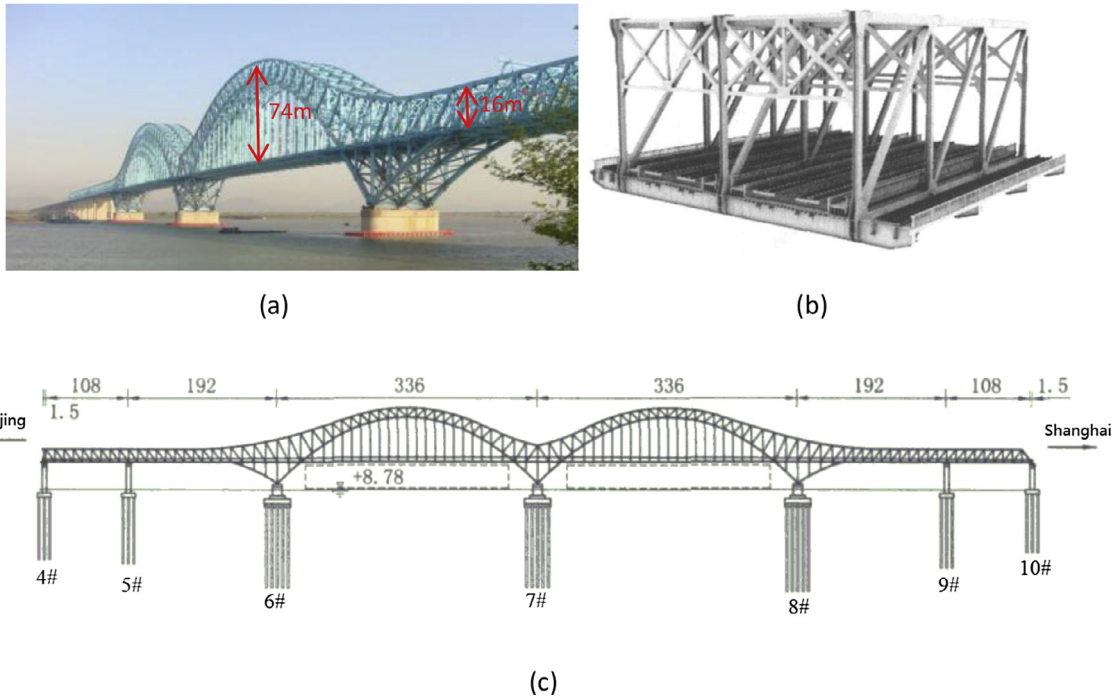
Fig. 2. Nanjing Dashengguan Yangtze River high-speed railway bridge. (a) Photograph of the bridge; (b) detail of the structure; (c) layout of the main bridge.

with the separation of the deformation and the thermal expansion components. It is worth noting that these works are based on X-band data. In fact, due to the short wavelength and the high spatial resolution of these data, they are particularly sensitive to thermal expansion. By contrast, there are significantly fewer studies that describe the thermal expansion observed using C-band Sentinel-1 data.

In this paper, the thermal expansion of a long-span high-speed railway is analysed. A dataset of C-band Sentinel images over the Nanjing Dashengguan Yangtze River high-speed railway bridge was processed. The longitudinal displacements of the entire bridge with a time span of more than one year were obtained. A correlation model between the displacements and the ambient temperature at each movable bearing (see Fig. 1) was derived, which was compared with the model based on in situ measurements. The bridge health status was evaluated based on the model and dozens of PSI measurement points located near each pier.

2. PSI phase components of the railway bridge

Monserrat et al. (2011) propose an extended PSI model which includes a phase component to capture the displacements related to temperature changes. Here we rewrite the model as follows:

$$\Delta\Phi^k = \frac{4\pi}{\lambda}\Delta t^k v + \frac{4\pi}{\lambda}\frac{B^k}{R^k\sin\theta^k}\Delta_{DEM} + \frac{4\pi}{\lambda}\Delta T^k\Delta_{The} + \Delta\Phi res^k \qquad (1)$$

where v, Δ_{DEM} and Δ_{The} are three unknowns that are contained in the linear displacement velocity, the DEM error and the thermal dilation phase components; $\Delta\Phi^k$ is the differential wrapped phase of the kth interferogram, Δt^k and B^k are the temporal and normal baselines, ΔT^k is the difference of temperature between the two acquisitions, R^k and θ^k are the slant range and incidence angle of the kth interferogram, λ is the radar wavelength, and $\Delta\Phi res^k$ is the residual phase. The extended model is more accurate than the two-parameter model used in the standard PSI techniques, because it explains the behaviour of the PSI observations using three components, and hence, the three unknown parameters. To properly estimate the three components, an appropriate number of SAR images is needed and no significant correlation between the temporal, spatial, and temperature-based baselines is required (Monserrat et al., 2011).

In this work, 29 Sentinel-1 SAR images were used to run the above extended model. Unfortunately, the available dataset proved insufficient to properly estimate the three components. In particular, the displacement velocity and the DEM error components could not be properly separated. For this reason, we decided to

carry out a simplified PSI approach, by considering that the dominant component of the observed interferometric phases is due to thermal expansion. In fact, according to existing displacement measurement on the piers (Wang et al., 2016; Zhou, 2015), the horizontal displacements due to thermal expansion of the bridge exceed 1 dm.

3. Displacement monitoring of the Dashengguan bridge

3.1. Overview of the Dashengguan bridge

The Dashengguan Yangtze River Bridge was completed in September 2009. It is a high-speed railway bridge located in Nanjing, China, 1 km upstream from the Nanjing Yangtze River Highway Bridge. The main part of the bridge has six (6) segments, which are (108 + 192 + 336 + 336 + 192 + 108) m long. The design size of 336 m ranks it as the world's longest high-speed railway. The layout of the bridge truss includes two tracks of the Beijing-Shanghai high-speed lines, on which trains reach speeds of 300 km/h, two tracks of the Shanghai-Chengdu railway lines, and two tracks of the Nanjing Metro. The bridge and the overall layout of the main structure are shown in Figs. 1 and 2.

3.2. SAR data and PSI processing

Twenty-nine (29) ascending Sentinel-1A images, acquired between April 25, 2015 and August 5, 2016, were used to analyse the longitudinal displacement of the bridge. See Table 1 for details.

Table 1
Line of Sight (LOS) deformation time series of the Dashengguan Yangtze River Bridge.

No.	Date	LOS Deformation/rad	T/°C	Max/rad	Min/rad
1	2015/4/25		25.0	0.00	0.00
2	2015/7/6		18.2	3.85	−3.40
3	2015/7/30		33.0	5.99	−4.63
4	2015/8/11		27.5	2.51	−1.45
5	2015/8/23		27.5	1.82	−2.03
6	2015/9/16		25.2	1.35	−1.02
7	2015/9/28		26.3	1.80	−1.37
8	2015/10/10		19.6	3.25	−3.55
9	2015/10/22		22.6	2.52	−1.64
10	2015/11/3		15.8	6.13	−5.64
11	2015/11/15		17.1	6.83	−5.10
12	2015/11/27		4.5	14.00	−13.50
13	2015/12/9		10.3	10.20	−10.73
14	2015/12/21		7.0	12.65	−13.45
15	2016/1/14		3.6	14.39	−13.91
16	2016/1/26		4.8	14.31	−14.69
17	2016/2/19		12.6	8.51	−9.49
18	2016/3/2		16.6	7.13	−9.33
19	2016/3/14		11.8	8.07	−9.93
20	2016/3/26		11.3	8.82	−10.03
21	2016/4/7		17.8	6.26	−6.62
22	2016/4/19		21.0	2.47	−2.71
23	2016/5/1		26.8	1.62	−1.85
24	2016/5/13		18.4	4.52	−4.36
25	2016/5/25		27.7	1.67	−1.67
26	2016/6/6		24.9	2.28	−1.27
27	2016/6/30		30.7	4.31	−2.83
28	2016/7/24		36.3	8.11	−7.69
29	2016/8/5		29.7	4.09	−3.54

-15   rad   +15

Beijing   Shanghai

4#   5#   6#   7#   8#   9# 10#

The first steps of the PSI processing were image co-registration and interferogram generation. The 1st image of the image stack was selected as super-master (SM), and the entire stack of SAR images was co-registered and resampled to the SM image geometry. A redundant network of 81 interferograms was generated, based on the co-registered images. The topographic phase in each interferogram was removed using the 3-arc SRTM DEM (Rabus et al., 2003). Multi-looking was not applied to preserve the original resolution of the data.

A mask covering the bridge was applied to constrain the propagation of phase unwrapping errors. Overall, 1828 pixels were selected at this stage. A threshold of 0.2 for the dispersion of amplitude was applied (Ferretti et al., 2001), and a 2 + 1D phase unwrapping algorithm was used for phase unwrapping (Crosetto et al., 2011). The advantage of this algorithm, which exploits the redundant network of interferograms, is the ability to perform a phase consistency check, correcting the pixels affected by unwrapping errors. After the 2 + 1D phase unwrapping step, the phases were transformed in displacements and referred to a reference point located in 7#.

Fig. 3(a) illustrates the mean amplitude image covering the Dashengguan railway bridge and the 3rd Nanjing highway bridge (in the lower right corner); Fig. 3(b) shows the differential interferogram of the 2016/03/26 and 2016/04/07 image pair. A comparison of the interferometric fringes of the two bridges reveals that the railway bridge with its truss structure has a clearer, more continuous pattern, while less coherent pixels are found on the highway bridge, which has asphalt pavement; the fringe pattern is masked by the phase noise of the water.

The LOS deformation evolution of the entire bridge is shown in Table 1. The deformation on the two sides of the bridge is almost equal, but in opposite directions (the average absolute difference value of the maximum and minimum deformation is 0.07 rad), while the magnitude of the deformation becomes larger with the distance from the bridge centre. The reference temperature (first image) is 25 °C. The red colours, with positive values, mean that the bridge is moving away from the satellite, while the blue colours, with negative values, imply that the movement is approaching the satellite. Considering the temperature of each image acquisition, the expansion and contraction of the bridge can be clearly identified.

Fig. 4 shows the imaging geometry of Sentinel-1A data at the Dashengguan bridge. Assuming the LOS deformation is only caused by the longitudinal displacement along the bridge, a simplified conversion of the LOS displacements into longitudinal displacements is given by the following equation:
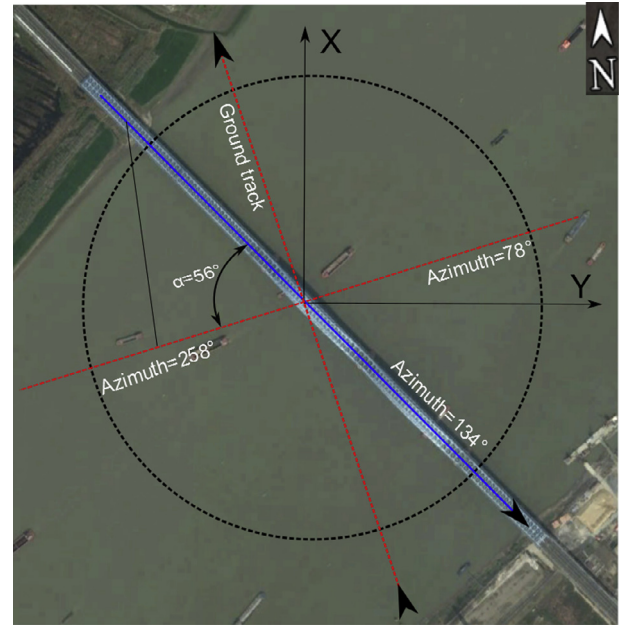
Fig. 4. Sentinel-1A ascending imaging geometry of the Dashengguan Bridge and LOS decomposition.

$$d_L = \frac{d_{LOS}}{\sin\theta\cos\alpha} \tag{2}$$

where d_{LOS} is the displacement in the LOS direction, d_L is the longitudinal displacement of the bridge, θ is the satellite incidence angle, which is 45°, and α is the horizontal angle between the longitudinal orientation of the bridge and the satellite LOS direction projected on the ground.

3.3. Correlation of displacements and temperatures

After the conversion of LOS displacements into the longitudinal direction of the bridge, done using equation (2), the displacements of all the selected pixels were obtained. In Fig. 5, we show the displacements along the AB profile indicated in Fig. 2. The ambient temperature of each image acquisition is plotted on the map (green diamonds), together with the position of the seven piers (red dots). This figure illustrates the longitudinal displacements as a function of the ambient temperature.
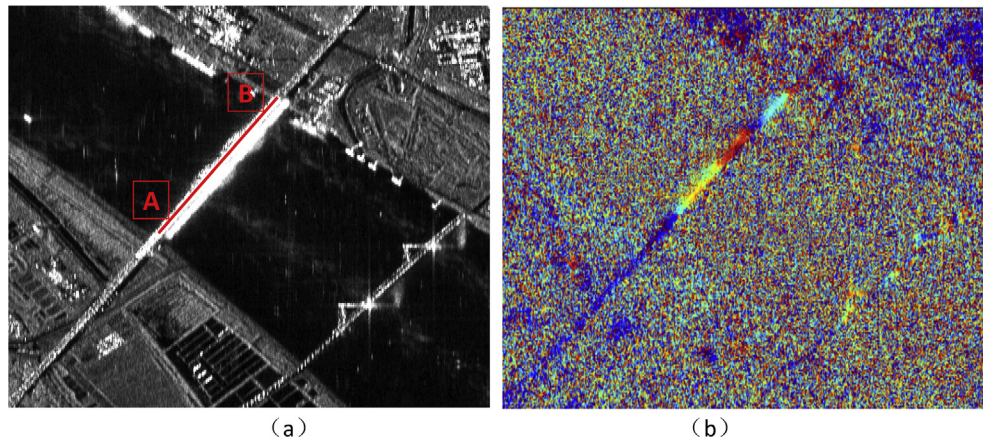
Fig. 3. Mean amplitude (a) and differential interferogram of the image pair 2016/03/26 and 2016/04/07 (b).
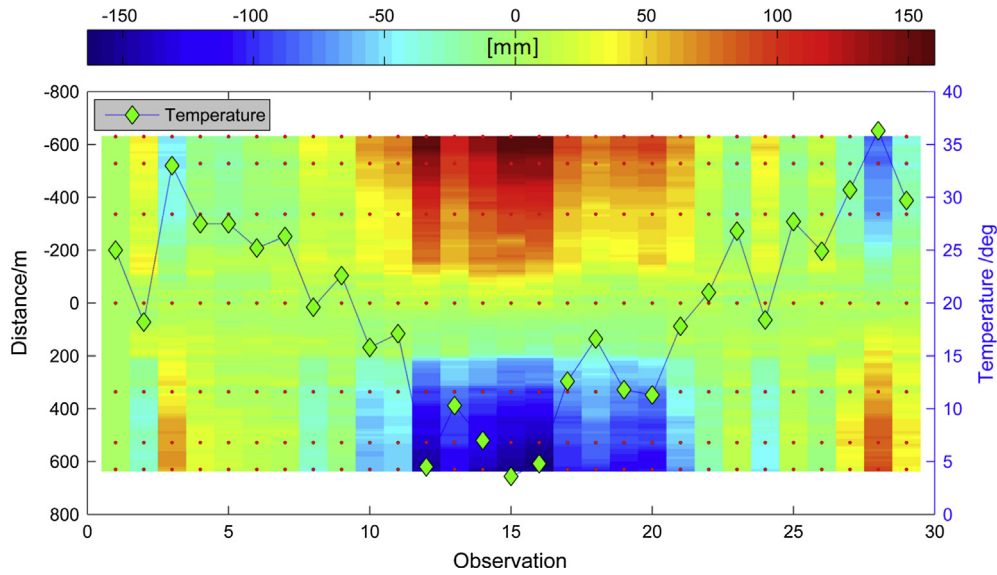
Fig. 5. Longitudinal displacements at each observation (SAR image) along the profile AB shown in Fig. 2, and corresponding temperature of each image acquisition (green rhombus). (For interpretation of the references to colour in this figure legend, the reader is referred to the web version of this article.)
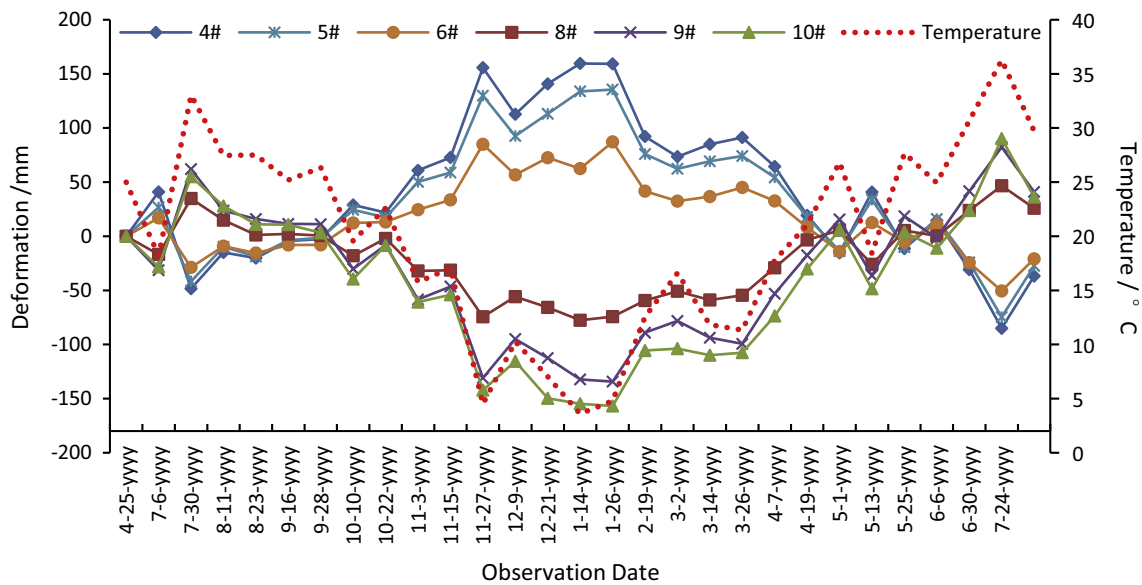
Fig. 6. Longitudinal displacement time series at six piers and image acquisition temperatures.

Fig. 6 shows the longitudinal displacement time series at the six piers along the profile AB and the temperature time series at each image acquisition time. The seasonal characteristic of the displacement variation is evident. Furthermore, the opposite correlation pattern of the temperature and the displacement time series, on both sides of the bridge, is also clear: where 8#, 9# and 10# have a positive correlation (0.98, 0.99, 0.98), 4#, 5# and 6# have a negative correlation (−0.99, −0.99, −0.98).

4. Analysis of displacements

A number of monitoring methods and a complex set of analyses are necessary to determine the health condition of a high-speed railway bridge. Among them, the performance of movable bearings is one of the key aspects to be analysed. To enable such analysis, it is necessary to carry out long-term monitoring and evaluation of the bearing state, assessing the bearing performance degradation, in order to repair or replace the damaged bearings in a timely manner. We can compute the following linear regression model at each pier:

$$d_L = b_0 + b_1 T \tag{3}$$

where d_L is the longitudinal displacement, T is the ambient temperature at the image acquisition time and b_0 and b_1 are the unknown regression parameters.

Fig. 7 shows the established model and the correlation for piers 4#, 5# and 6# on the northwest side of the Dashengguan high-speed railway bridge. In Zhou (2015), the longitudinal displacements and the structural temperatures measured in-situ, which were collected at 10-min intervals from March 2013 to October 2013, were used to estimate the reference model parameters. The InSAR and the reference models are compared in Table 2.
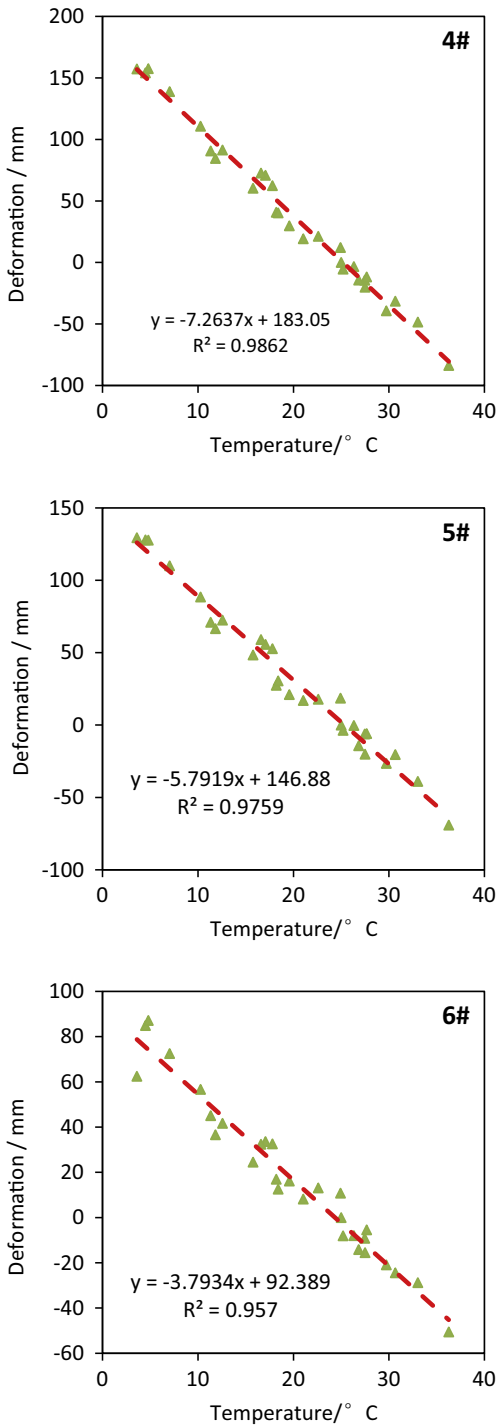
Fig. 7. Linear regression model of the longitudinal displacements with respect to the ambient temperatures at piers 4#, 5# and 6#.

Table 2
Regression models (InSAR and reference) of deformations along the bridge and temperatures at piers 4#, 5# and 6#.

Pier	Ref Model	InSAR Model	Diff/mm/°C
4#		$d_L = 115.24 - 6.96T$	
		$d_L = 183.05 - 7.26T$	0.30
5#	$d_L = 92.53 - 5.62T$	$d_L = 146.88 - 5.79T$	0.17
6#	$d_L = 66.28 - 3.82T$	$d_L = 92.24 - 3.79T$	−0.03

The differences of the slopes between the two models are 0.30 mm/°C, 0.17 mm/°C and −0.03 mm/°C respectively: there is good agreement between the two models.

5. Bridge health evaluation

Once the displacement model at each pier is established, the bridge's health can be evaluated using confidence and prediction intervals. In fact, the displacement model can be built at the beginning of the bridge life by InSAR, or other traditional methods, such as the above mentioned in-situ measurements. In our case, let's
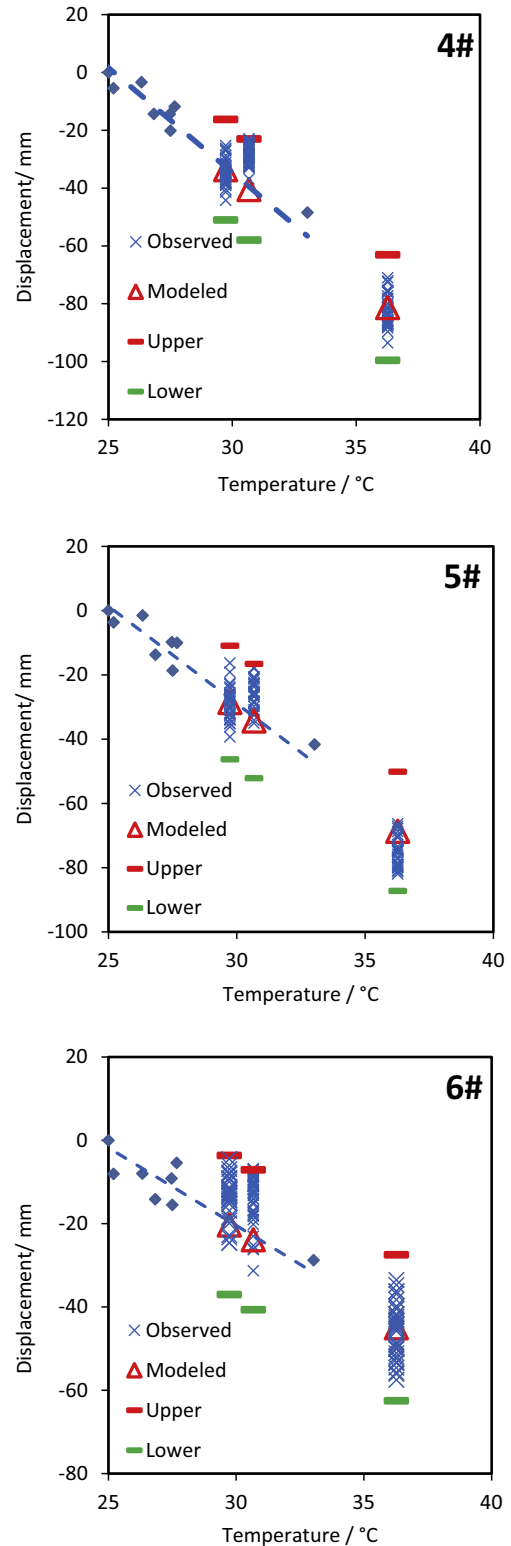
Fig. 8. Longitudinal displacements measured and modelled at movable bearing 4#, 5# and 6#.

Table 3
Longitudinal displacements measured and modelled at 4#, 5# and 6#.

Pier	Temp./°C	Modelled/mm	Mean obs./mm	Diff./mm	[Min, Max] obs./mm	[Upper, Lower]/mm	In. Perc./%
4#	30.7	−40.5	−28.6	11.9	[−36.9,−23.1]	[−58.0,−23.0]	100
	36.3	−81.3	−82.4	−1.1	[−93.5,−71.0]	[−99.6,−63.1]	100
	29.7	−33.6	−34.6	−1.0	[−44.2,−25.3]	[−51.0,−16.2]	100
5#	30.7	−34.4	−26.6	−7.8	[−35.0,−17.6]	[−52.1,−16.6]	100
	36.3	−68.7	−75.3	−6.6	[−82.0,−66.3]	[−87.2,−50.1]	100
	29.7	−28.6	−29.1	−0.5	[−39.3,−16.3]	[−46.3,−10.9]	100
6#	30.7	−23.9	−14.1	−9.8	[−31.3,−6.8]	[−40.6,−7.1]	93
	36.3	−45.0	−45.7	0.7	[−57.5,−33.5]	[−62.5,−27.5]	100
	29.7	−20.3	−13.6	−6.7	[−24.6,−4.5]	[−37.0,−3.6]	100

assume that the regression model is given by formula (3) at each pier, and a total number of M images were used for the estimation of the model parameters, with a mean square error of the estimates MS_{Res}. For an additional SAR acquisition, with ambient temperature T_{M+1}, we have the predicted longitudinal displacements $\hat{d}_L$, which are calculated by fomula (3). An unbiased estimate of the standard error (stdev) of $\hat{d}_L$, called the standard error of the fit, is given by the formula

$$stdev = \sqrt{MS_{Res} \cdot X_0^T (X^T X)^{-1} X_0} \qquad (4)$$

where X is the $M \times 2$ matrix whose rows are $(1, T_1), (1, T_2), \ldots, (1, T_M)$, and X_0 is $(1, T_{M+1})^T$.

The $1 - \alpha$ confidence interval for the true value of $\hat{d}_L$ is therefore $\hat{d}_L \pm t_{crit} \Delta \cdot stdev$, where t_{crit} is the critical value of the t distribution with degrees of freedom $df_{Res} = M - 1$ and with significance level $\alpha/2$. The prediction interval is calculated in a similar way, except that now the variance is the variance of the residual $d_L - \hat{d}_L$, which is:

$$MS_{Res} + MS_{Res} \cdot X_0^T (X^T X)^{-1} X_0 \qquad (5)$$

The $1 - \alpha$ confidence interval of $\hat{d}_L$ is therefore:

$$\hat{d}_L \pm t_{crit} \cdot \sqrt{MS_{Res}(1 + X_0^T (X^T X)^{-1} X_0)} \qquad (6)$$

Here the last term is called the standard deviation of the prediction.

Let's take the movable bearings 4#, 5# and 6# for example, to evaluate their health status, assuming that the bearings were working well before the 26th image acquisition date. We used the first 26 images to build the linear models (see the blue diamonds and the fitted blue dashed lines in Fig. 8). Then the modelled values for the next three measurements, which are marked with red triangles, were calculated with the image acquisition temperatures: their 0.95 confidence intervals are illustrated with red[1] (upper band) and green (lower band) symbols. As for the measured displacements, pixels in a 7-pixel radius were selected at each pier, which are marked with blue x's in Fig. 8. The number of measurements is very similar in 4# and 5#: 37 and 32 respectively. In 6# the number is 40. Detailed longitudinal measurements and predicted results are listed in Table 3. The columns of the table include pier number, temperatures of observation, modelled value calculated with formula (3), mean value of all the PSI measurements near each pier, the difference between the modelled and mean value, minimum and maximum PSI observation, lower upper band of predicted value with 0.95 confidence, and percentage of observed PSI inside the intervals. From the table we can see that (1) nearly all the measured displacements are in the predicted intervals, and the

percentage for 4# and 5# is 100%. A partial exception is given by 6# (93%), where 3 out of 40 measurements are out of the boundaries, even though they are very close to the upper band limit, and (2) all averaged displacements at each pier are included in the predicted intervals. From the results we can conclude that the movable bearings have a good working status with a confidence of 95%. If the observed displacements were not within the intervals (as said, this could partially be the case of 6#), a further analysis of the bearings would be required.

6. Discussion and conclusion

Thermal expansion is a significant component in steel truss bridge displacements. In this work a PSI technique has been used for the longitudinal displacement monitoring of a railway bridge. Twenty-nine ascending C-band Sentinel-1A images have been analysed. A total of 1828 PS points have been selected and used for the PSI time series analysis.

The estimated longitudinal displacements of the Nanjing Dashengguan high-speed railway bridge measure up to 150 mm. The displacements reveal a high correlation with the ambient temperature: a negative correlation (−0.99, −0.99, −0.98) at piers 4#, 5# and 6#, and a positive correlation (0.98, 0.99, 0.98) at piers 8#, 9# and 10#.

The regression models of the longitudinal displacements versus the ambient temperatures have been computed. The results show a good agreement with the reference models built using in-situ measurement carried out at the movable bearings. The status of the movable bearings was evaluated based on regression models and using confidence and prediction intervals. This demonstrated the capability of C-band Sentinel data for structural health monitoring of long-span high-speed railway bridges. It is worth noting that in this study ambient temperatures were used. More accurate temperatures, directly related to the studied structure, should be acquired to improve displacement modelling.

As of November 1, 2016, 21,688 km of high-speed railways are in operation in mainland China, accounting for more than 60% of such railways in the world (UIC, 2016). Most of the high-speed railways are built in the form of bridges or viaducts (e.g., 86.5% of the high-speed railway from Beijing to Shanghai is made up of bridges). The conditions of the high-speed railway bridges must be regularly monitored. Nowadays, only field campaigns are used for railway bridge displacement monitoring. The potential advantages of Sentinel-1 data for high-speed railway bridge monitoring at the continental scale is evident. Sentinel-1 acquires data with a swath of 240 km and the area coverage of a single image is approximately 45,000 km^2. This wide area coverage has the potential of monitoring bridges throughout the entire country with a frequency of 12 days with Sentinel-1A alone, and six days using both Sentinel-1A and -1B. Another advantage of the InSAR and PSI techniques is the ability to perform remote monitoring: with Sentinel-1 SAR data the bridges could be monitored with no need for

---

[1] For interpretation of color in Fig. 8, the reader is referred to the web version of this article.

laborious in-situ observations. The third advantage of SAR interferometry is its high density: a lot of points along bridge can be obtained to monitor the entire bridge, not only at the movable bearings, as is the case with in-situ monitoring.

Acknowledgements

References

Crosetto, M., Biescas, E., Duro, J., Closa, J., Arnaud, A., 2008. Generation of advanced ERS and Envisat interferometric SAR products using the stable point network technique. Photogramm. Eng. Remote Sens. 74 (4), 443–450.

Crosetto, M., Gili, J.A., Monserrat, O., Cuevas-González, M., Corominas, J., Serral, D., 2013. Interferometric SAR monitoring of the Vallcebre landslide (Spain) using corner reflectors. Nat. Hazards Earth Syst. Sci. 13 (4), 923–933.

Crosetto, M., Monserrat, O., Iglesias, R., Crippa, B., 2010. Persistent scatterer interferometry: potential, limits and initial C- and X-band comparison. Photogramm. Eng. Remote Sens. 76 (9SI), 1061–1069.

Crosetto, M., Monserrat, O., Cuevas, M., Crippa, B., 2011. Spaceborne differential SAR interferometry: data analysis tools for deformation measurement. Remote Sens. 3 (12), 305–318.

Crosetto, M., Monserrat, O., Cuevas-Gonzalez, M., Devanthery, N., Crippa, B., 2016. Persistent scatterer interferometry: a review. ISPRS J. Photogramm. Remote Sens. 115, 78–89.

Cuevas, M., Monserrat, O., Crosetto, M., Crippa, B., 2011. A new product from persistent scatterer interferometry: the thermal dilation maps. In: JURSE 2011, Munich, Germany.

Dai, K., Liu, G., Li, Z., Li, T., Yu, B., Wang, X., Singleton, A., 2015. Extracting vertical displacement rates in Shanghai (China) with multi-platform SAR images. Remote Sens. 7 (8), 9542–9562.

de Battista, N., Westgate, R., Koo, K.Y., Brownjohn, J., 2011. Wireless monitoring of the longitudinal displacement of the Tamar Suspension Bridge deck under changing environmental conditions. In: Proceedings of SPIE-The International Society for Optical Engineering, Bellingham.

Eineder, M., Adam, N., Bamler, R., Yague-Martinez, N., Breit, H., 2009. Spaceborne Spotlight SAR interferometry with TerraSAR-X. IEEE Trans. Geosci. Remote Sens. 47 (5), 1524–1535.

Ferretti, A., Prati, C., Rocca, F., 2001. Permanent scatterers in SAR interferometry. IEEE Trans. Geosci. Remote Sens. 39 (1), 8–20.

Fornaro, G., Reale, D., Verde, S., 2013. Bridge thermal dilation monitoring with millimeter sensitivity via multidimensional SAR imaging. IEEE Geosci. Remote Sens. Lett. 10 (4), 677–681.

Gernhardt, S., Adam, N., Eineder, M., Bamler, R., 2010. Potential of very high resolution SAR for persistent scatterer interferometry in urban areas. Ann. GIS 16 (2), 103–111.

Goel, K., Rodriguez Gonzalez, F., Adam, N., Duro, J., 2014. Thermal dilation monitoring of complex urban infrastructure using high resolution SAR data. In: IGARSS 2014, pp. 954–957.

Lazecky, M., Hlavacova, I., Bakon, M., Sousa, J.J., Perissin, D., Patricio, G., 2016. Bridge displacements monitoring using space-borne X-band SAR interferometry. IEEE J. Sel. Top. Appl. Earth Observ. Remote Sens., 1–6

Lin, H., Chen, F., Jiang, L., Zhao, Q., Cheng, S., 2010. Preliminary research on large-scale man-made linear features deformation monitoring using multi-baseline differential SAR interferometry. J. Geo-Inform. Sci. 12 (5), 718–725.

Liu, Y., Xu, C., Li, Z., Wen, Y., Chen, J., Li, Z., 2016. Time-dependent afterslip of the 2009 Mw 6.3 Dachaidan Earthquake (China) and viscosity beneath the Qaidam Basin inferred from postseismic deformation observations. Remote Sens. 8 (8), 649.

Monserrat, O., Crosetto, M., Cuevas, M., Crippa, B., 2011. The thermal expansion component of persistent scatterer interferometry observations. IEEE Geosci. Remote Sens. Lett. 8 (5), 864–868.

Perissin, D., Rocca, F., 2006. High-accuracy urban DEM using permanent scatterers. IEEE Trans. Geosci. Remote Sens. 44 (112), 3338–3347.

Rabus, B., Eineder, M., Roth, A., Bamler, R., 2003. The shuttle radar topography mission – a new class of digital elevation models acquired by spaceborne radar. ISPRS J. Photogramm. Remote Sens. 57 (4), 241–262.

Reale, D., Fornaro, G., Pauciullo, A., 2013. Extension of 4-D SAR imaging to the monitoring of thermally dilating scatterers. IEEE Trans. Geosci. Remote Sens. 51 (12), 5296–5306.

Tosi, L., Da Lio, C., Strozzi, T., Teatini, P., 2016. Combining L- and X-band SAR interferometry to assess ground displacements in heterogeneous coastal environments: the Po River Delta and Venice Lagoon, Italy. Remote Sens. 8 (4), 308.

UIC High Speed Department: High speed lines in the world, 2016, <http://uic.org/high-speed-database-maps#documents>.

Wang, G., Ding, Y., Song, Y., Wu, L., Yue, Q., Mao, G., 2016. Detection and location of the degraded bearings based on monitoring the longitudinal expansion performance of the main girder of the Dashengguan Yangtze Bridge. J. Perform. Construct. Facil. 30 (4). http://dx.doi.org/10.1061/(ASCE)CF.1943-5509.0000820.

Webb, G.T., Vardanega, P.J., Fidler, P.R.A., Middleton, C.R., 2014. Analysis of structural health monitoring data from hammersmith flyover. J. Bridge Eng. 19 (6), 213–226.

Wen, Y., Xu, C., Liu, Y., Jiang, G., 2016. Deformation and source parameters of the 2015 Mw 6.5 earthquake in Pishan, western China, from Sentinel-1A and ALOS-2 data. Remote Sens. 8 (1342).

Yi, T., Li, H., Gu, M., 2010. Recent research and applications of GPS based technology for bridge health monitoring. Sci. China-Technol. Sci. 53 (10), 2597–2610.

Zhou, K., 2015. Research on State Evaluation and Early Warning Method of Bridge Structure based on Monitoring Data. Southeast University.